Broadband frequency control of light using synthetic frequency lattices formed by four-wave-mixing Bragg scatterings

Wenwan Li,[1,*] Ningning Yang,[1,*] Hao Chen,[1,*] Bing Wang,[1,†] Chengzhi Qin,[1] Tianwen Han,[1] Yicong Zhang,[1] Weiwei Liu,[1] Chi Zhang,[1,‡] Xinliang Zhang,[1] and Peixiang Lu[1,2,3,§]

[1]*Wuhan National Laboratory for Optoelectronics and School of Physics, Huazhong University of Science and Technology, Wuhan 430074, China*

[2]*Hubei Key Laboratory of Optical Information and Pattern Recognition, Wuhan Institute of Technology, Wuhan 430205, China*

[3]*CAS Center for Excellence in Ultra-intense Laser Science, Shanghai 201800, China*

(Received 14 December 2020; accepted 9 March 2021; published 22 March 2021)

Recent exploration in synthetic frequency lattices has re-formed the methods of manipulating the light spectrum by analogizing the diffraction management in real space, which can be created by employing electro-optic modulation (EOM) in dielectric waveguides or ring resonators. In the presence of effective gauge potential, that is, the accumulated phase of mode transfer between adjacent lattice sites, the frequency spectrum of incident light can be flexibly tailored. However, the finite bandwidth and modulation depth of EOM vastly restrain the frequency shift and efficiency of mode transfer. Here we experimentally demonstrate that the synthetic frequency lattice can be created with the nonlinear process of four-wave-mixing Bragg scattering. The bandwidth of frequency manipulation is expanded up to terahertz and the frequency shift can be larger than 200 GHz. Furthermore, we can realize effects such as negative refraction and perfect imaging in frequency dimension by changing the effective gauge potentials. The study provides a powerful and promising approach to precisely control light frequency in broadband and may benefit all-optical modulation in optical telecommunication systems.

DOI: 10.1103/PhysRevA.103.033514

I. INTRODUCTION

Precise and broadband frequency control of light is generally a crucial technique in optical science and engineering. With the invention of optical frequency combs (OFCs) [1–5], which describe the spectra of phase-coherent evenly spaced frequency lines, versatile methods for manipulating light frequencies have been explored. For example, controlling the intensity and phase modulations of individual comb lines can benefit line by line phase shaping in optical arbitrary waveform generation [6]. So far OFCs have found great applications ranging from time and frequency metrology [7–9] to optical telecommunication [10–12] and molecular spectroscopy [13–15], where the manipulation of OFCs has always played the key role in basic technology.

In terms of the frequency spectrum, OFCs are constituted by a series of discrete modes with identical frequency spacing and phase difference between the comb lines [16]. For an OFC with unlimited bandwidth and uniform amplitude of comb lines, its spectrum is well defined by a Bloch wave function in frequency dimension, which can evolve in synthetic frequency lattices (SFLs) as eigenmodes, analogous to their spatial counterparts in optical waveguide arrays [17,18]. Synthetic lattices expand the concept of spatial lattices to arbitrary parameter spaces and offer unique platforms to manipulate light in various dimensions such as time [19–21], frequency [22–25], and angular momentum [26–29]. The SFLs were originally created in ring resonators and dielectric waveguides under dynamical modulation based on the electro-optical effect, where the modes with distinct frequencies could transfer to each other [30–32]. The accumulated phase change during mode transfer corresponds to an effective gauge potential for photons. In analogy with vector potential applied to electrons, the effective gauge potential provides great opportunities to control the frequency of light [33–35].

Apart from electro-optic modulation, the SFLs can also be created by using the nonlinear effect [36–40]. Comparing with the electro-optical effect possessing a typical modulation frequency of 10 GHz, the nonlinear approach provides an all-optical scheme to manipulate frequency, which manifests a much faster optical response [41]. Furthermore, the modulation frequency could increase remarkably by several times higher than the electromagnetic effect, leading to a broadband control of light frequencies [42].

In this paper, we shall experimentally construct a SFL in an optical fiber communication system based on the nonlinear effect of four-wave-mixing Bragg scattering (FWM-BS). The lattice has a frequency spacing larger than 100 GHz and benefits broadband and precise control of light frequency. By introducing the gauge potential via adjusting the phase delay

*These authors contributed equally to this work.
†wangbing@hust.edu.cn
‡chizheung@hust.edu.cn
§lupeixiang@hust.edu.cn

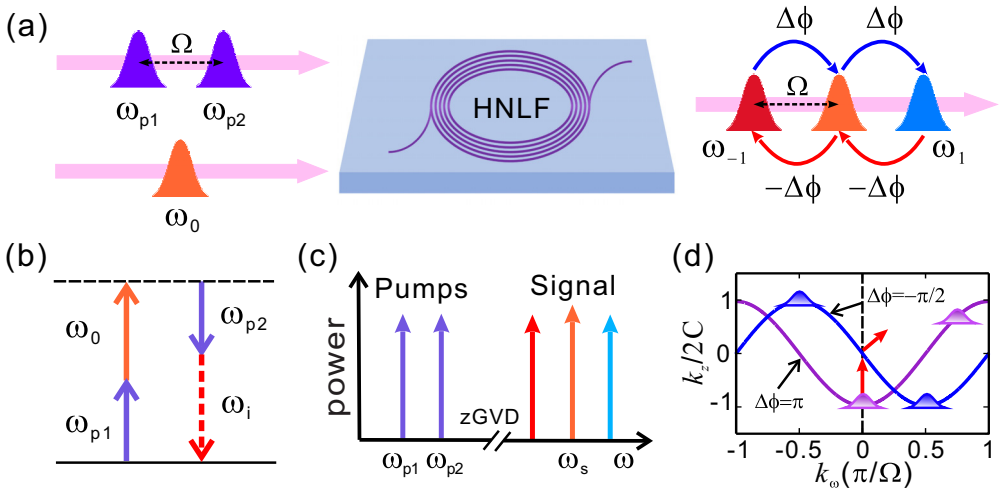

FIG. 1. (a) Generation of SFL by FWM-BS process in nonlinear fiber system. $\omega_{p1,2}$ and ω_0 represent the frequency of the incident pumps and signal. The frequency difference Ω of the two pumps provides the frequency interval of the lattice. $\Delta\phi$ is the phase difference of two pumps. The distinct coupling direction is denoted by the blue and red arrows. (b) Photon picture of the FWM-BS process. ω_i is the idler frequency. (c) Phase-match condition. The wavelength of zero group velocity dispersion (z-GVD) needs to be between the optical signal and the pump. (d) Band structures of the lattice for $\Delta\phi = -\pi/2$ and $\Delta\phi = \pi$. The red arrows denote the direction of group velocity at Bloch wave vector $k_\omega = 0$.

of pumping light, we can conveniently realize frequency shift for incidence of OFCs, although the frequency diffraction occurs for a truncated bandwidth. The shift of the spectrum approaches as large as 200 GHz, which is five times larger than that achieved by electro-optic modulations. The direction of the shift is controllable by employing two processes of FWM-BS with different gauge potentials. For a single frequency incidence, the frequency scaling and imaging are both achieved. The study provides another powerful and promising approach to control precisely light frequency over a broadband using a nonlinear process.

II. THEORETICAL MODEL

The FWM-BS process is implemented in a highly nonlinear fiber (HNLF), as shown in the schematic diagram of Fig. 1(a). An optical signal at frequency ω_0 is scattered by two pumps with frequencies ω_{p1} and ω_{p2} resulting in the generation of idlers with frequencies $\omega_i = \omega_0 \pm \Omega$. After successive FWM-BS processes, the signal will undergo a series of up- or downshifts, forming a SFL with lattice constant $\Omega = \omega_{p1} - \omega_{p2}$. Specially, in the FWM-BS process, each idler photon is generated from an annihilated signal photon and the power directly transfers from the signal to the idler, as depicted in Fig. 1(b). This avoids the amplification of vacuum fluctuation caused by the additional noise during the parametric gain process. Therefore, the FWM-BS process enables us to achieve a low-loss frequency conversion [43–45].

The total electric field in the nonlinear medium can be written as [46]

$$U = \sum_{n=-\infty}^{\infty} a_n(z)e^{-i\omega_n t} + A_1 e^{-i(\omega_{p1}+\phi_1)} + A_2 e^{-i(\omega_{p2}+\phi_2)}, \quad (1)$$

where $a_n(z)$ is the amplitude of the idlers at frequency ω_n. $\phi_{1,2}$, respectively, represent the initial phases of the pumps. The amplitudes of the two pumps are denoted by $A_{1,2}(z)$. To satisfy the phase-match condition, the frequencies of the two pumps and signal should be close to the equidistant sides of the zero dispersion wavelength, as shown in Fig. 1(c). In this case, the pumps and signal will move at the same group velocity and the group velocity dispersion can be ignored. Taking advantage of the undepleted pump approximation in the process and substituting Eq. (1) into the nonlinear Schrödinger equation, we could obtain the coupled-mode equation with respect to the idlers,

$$\frac{\partial a_n}{\partial z} = iC[a_{n-1}(z)e^{i\Delta\phi} + a_{n+1}(z)e^{-i\Delta\phi}], \quad (2)$$

where $C = 2\gamma A_1(0)A_2(0)$ denotes the coupling strength, and $A_{1,2}(0)$ are the amplitudes of the incident pumps. $\Delta\phi = \phi_1 - \phi_2$ denotes the phase difference between the pumps. We note that the additional phase has the opposite signs for upward and downward transitions of photons. This nonreciprocal phase is the photonics analog of the electronic Peierls phase in the Aharonov-Bohm effect and is associated with the effective photonic gauge potential A_{eff} in SFL through [33–35]

$$\Delta\phi = \int_{\omega_n}^{\omega_{n+1}} A_{\text{eff}} d\omega, \quad (3)$$

where ω represents the frequency of the idler and the gauge potential could be expressed as $A_{\text{eff}} = \Delta\phi/\Omega$.

An infinite-width OFC can be regarded as the eigen Bloch mode in SFL $a_n(z) = a_0\exp(in\phi_0)\exp(ik_z z)$ with a_0 the amplitude for the nth modes, k_z the propagation constant along the z direction, and ϕ_0 the initial Bloch momentum in frequency dimension. By substituting $a_n(z)$ into Eq. (2), we can obtain the dispersion relation for the SFL:

$$k_z(\phi_0) = 2C\cos(\phi_0 - \Delta\phi). \quad (4)$$

Denoting $\phi_0 = k_\omega\Omega$, k_ω the initial Bloch wave vector, and considering $A_{\text{eff}} = \Delta\phi/\Omega$, the band structure can read

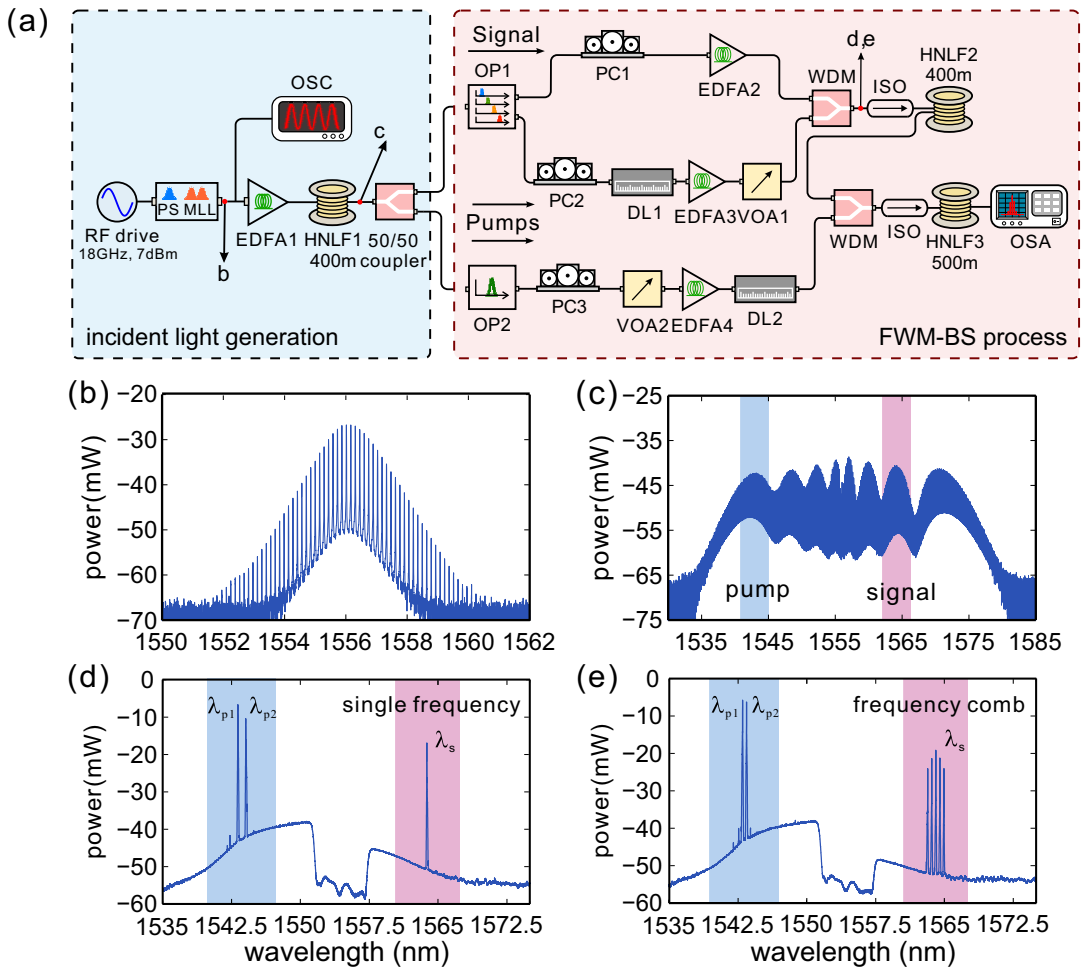

FIG. 2. (a) Experimental setup. PS MLL, picosecond mode-locked laser; OSC, oscilloscope; EDFA, erbium-doped fiber amplifier; HNLF, highly nonlinear fiber; OP, optical processor (Finisar WaveShaper 4000A and 1000S); PC, polarization controller; DL, delay line; VOA, variable optical attenuator; WDM, wavelength division multiplexer; ISO, isolator; OSA, optical spectrum analyzer. All the couplers in this system are 50/50 couplers. The red and blue lines represent the first and second FWM-BS processes. (b) Optical spectrum of the mode-locked laser. (c) Optical spectrum after HNLF1. (d) Optical spectrum for incidence of a single frequency. (e) Optical spectrum for incidence of OFC. The blue and pink areas in (c,d,e) indicate the ranges of the pumps and signal. λ_s and $\lambda_{p1,p2}$ are the wavelengths of signal and pumps.

$k_z(k_\omega) = 2C\cos[(k_\omega - A_{\text{eff}})\Omega]$. For a finite-width OFC, the group velocity which is perpendicular to the band structure in the frequency dimension can be expressed as

$$v_{g,\omega}(z) = -\frac{\partial k_z(k_\omega)}{\partial k_\omega} = 2C\Omega\sin(\phi_0 - \Delta\phi), \tag{5}$$

which leads to an accumulated frequency shift,

$$\Delta\omega = \int_0^L v_{g,\omega}dz' = 2m_d\Omega\sin(\phi_0 - \Delta\phi), \tag{6}$$

where $m_d = CL$ with L the propagation length.

It is apparent from Eq. (4) that the band structure undergoes a shift in the presence of the effective gauge potential. Thus, the propagation direction of group velocity will be different at the same Bloch momentum, as shown in Fig. 1(d). This motivates us to achieve the directional transmission and arbitrary refraction phenomena in the frequency dimension by cascading two FWM-BS processes with different pump phases.

III. RESULTS AND DISCUSSION

A. Experimental setup

The experimental setup for the two cascaded FWM-BS processes is shown in Fig. 2(a). The pumps and signal lights are generated by a picosecond mode-locked laser (MLL) driven by a sinusoidal radiofrequency (rf) signal. The repetition frequency and amplitude of the rf signal are 18 GHz and 7 dBm. The optical spectrum after MLL is shown in Fig. 2(b). During the experiment, the optical signal and pump both experience frequency conversion. For preventing the sidebands generated by the FWM-BS process from overlapping, the pumps and signal should be fully separated. To satisfy this condition, the spectrum of the mode-locked laser is expanded to more than 30 nm by self-phase modulation and FWM process in HNLF1 of 400 m. The wavelength interval between optical pump and signal reaches 20 nm, as presented in Fig. 2(c). The incident pumps and signal lights, whose spectra are shown in Figs. 2(d) and 2(e), are filtered out by OP1. OP2 is utilized to filter the pumps used in the second nonlinear

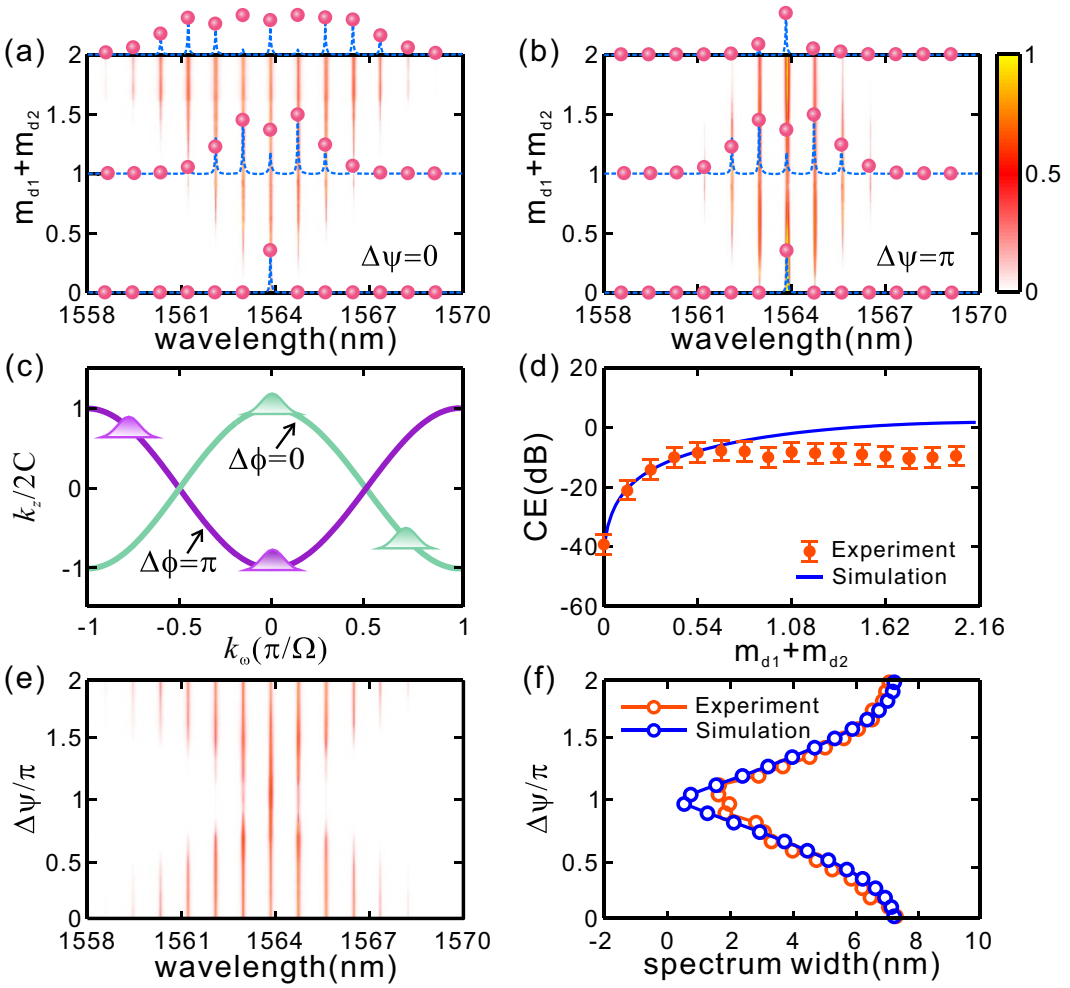

FIG. 3. (a), (b) Experimental results for $\Delta\psi = 0$ and $\Delta\psi = \pi$ in the case of single frequency input. $\Delta\psi = \Delta\phi_1 - \Delta\phi_2$. The frequency evolution varies with the total modulation depth $m_{d1} + m_{d2}$. The dashed covers and dots, respectively, represent the experimental and simulated results at the total modulation depth $m_d = 0$, 1, and 2. (c) Band structure of the frequency Bloch mode for $\Delta\phi = 0$ and $\Delta\phi = \pi$. (d) Experimental and simulated conversion efficiency of the total FWM-BS process with increasing modulation depth in the case of $\Delta\psi = 0$. (e) Output spectrum as a function of $\Delta\psi$ for single frequency input. (f) Experimental and simulated spectrum width when $\Delta\psi$ varies.

process. According to the zero-dispersion wavelength of the HNLF, the wavelength of the signal is $\lambda_s = 1563.79$ nm, the pump lights in the two nonlinear processes are all around 1544 nm, and the frequency difference of the two pumps is $\Omega = 108$ GHz. The two FWM-BS processes, respectively, occur in nonlinear fibers with lengths of 400 and 500 m. The final spectrum is detected by an optical spectrum analyzer (OSA). In the experiment, the signal and pumps are amplified by the erbium-doped fiber amplifier (EDFA). The power and phase difference of the two pumps are controlled by the variable optical attenuator (VOA) and delay line (DL), respectively. Three polarization controllers (PCs) are utilized for controlling the light polarization states in the HNLF to optimize the conversion efficiency of the FWM-BS process. During the measurement, we first only consider the FWM-BS process in HNLF2 and the modulation depth m_{d1} linearly increases from zero to its maximum. Then, we fix m_{d1} and increase the modulation depth m_{d2} to the same value as the m_{d1} in the second FWM-BS process. The modulation depths $m_{d1,d2}$ are controlled by varying the power of two pumps.

B. Discrete diffraction and perfect imaging in the frequency dimension

Figure 3(a) shows the experimental output spectrum when $\Delta\psi = \Delta\phi_1 - \Delta\phi_2 = 0$. With the total modulation depth $m_d = m_{d1} + m_{d2}$ linearly increasing, the power of the optical signal gradually transfers to the idlers and the spectrum exhibits discrete diffraction. However, as $\Delta\psi = \Delta\phi_1 - \Delta\phi_2 = \pi$ the frequency spectrum will be broadened first and then recover to its origin, as shown in Fig. 3(b). The dots and dashed lines in Figs. 3(a) and 3(b), respectively, denote the experimental and simulated results at $m_d = 0$, 1, and 2. The phenomena can be explained according to the band structure, as illustrated in Fig. 3(c). As $\Delta\phi_1$ and $\Delta\phi_2$ is in phase during the propagation, the band structure of the two FWM-BS processes always remains the same. Therefore, the direction of group velocity at the same Bloch momentum will be unchanged during the propagation, giving rise to "spectrum broadening." On the other hand, when $\Delta\phi_1 - \Delta\phi_2 = \pi$, the band structure of the second process undergoes a shift to the left in the Brillouin zone relative to the first process.

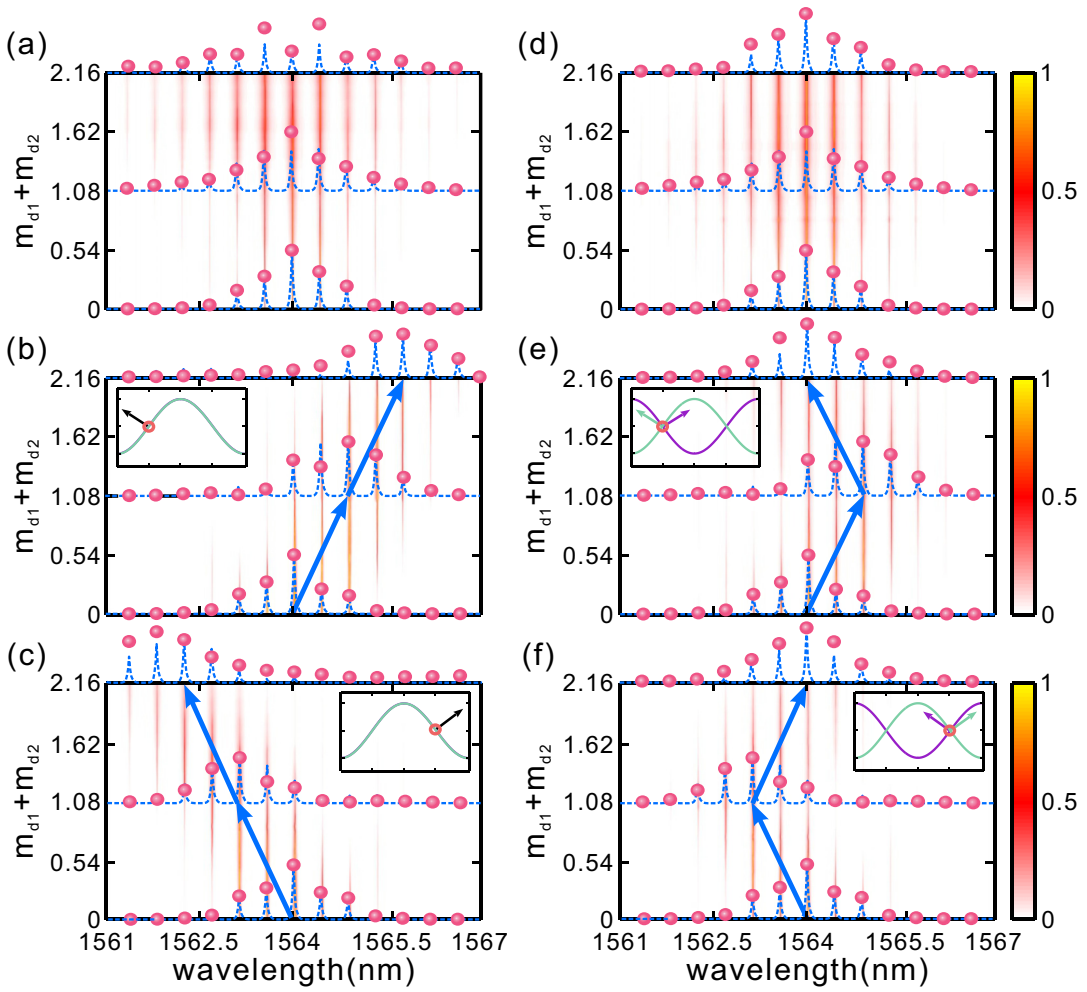

FIG. 4. (a)–(c) Experimental output spectrum vs total modulation depth as ϕ_0–$\Delta\phi_1 = 0$, $-\pi/2$, and $\pi/2$ for $\Delta\psi = 0$. ϕ_0–$\Delta\phi_1$ is the variation of the effective gauge potential with ϕ_0 the phase difference between two frequencies of the incident OFC and $\Delta\phi_1$ the phase difference of two pumps. (d)–(f) Experimental output spectrum vs total modulation depth as the initial phase ϕ_0–$\Delta\phi_1 = 0$, $-\pi/2$, and $\pi/2$ for $\Delta\psi = \pi$. The blue dashed curves and pink dots, respectively, represent the experimental and simulated results at the total modulation depth $m_d = 0$, 1.08, and 2.16. The red arrows represent the direction of frequency shift. The insets in (b), (c), (e), (f) show the calculated band structure for the first (green) and second (purple) FWM-BS processes. The arrows in the insets denote the direction of group velocity.

The group velocity at the same Bloch momentum is opposite in the lateral direction during the two FWM-BS processes. Consequently, the spectrum exhibits the perfect imaging in the frequency domain. Figure 3(d) depicts the conversion efficiency as a function of total modulation depth in the case of $\Delta\psi = \Delta\phi_1 - \Delta\phi_2 = 0$. The conversion efficiency is defined as the converted idler photon at the fiber output divided by the input signal photon at the fiber input. The measured and simulated results both show that the conversion efficiency gradually increases as m_d gets higher. When m_d is low, the measured conversion efficiency is consistent with the simulation. However, with further increasing m_d, the simulation is going to be higher than the measured conversion efficiency because of the loss of the fiber. Therefore, the signal cannot convert to the idlers entirely which causes the power of the signal and the nth idlers will not decrease to zero in the experiment. Furthermore, we fix $m_{d1} = m_{d2} = 1$ in the two processes and continually vary the delay lines to change $\Delta\psi$ from 0 to 2π. The influence of $\Delta\psi$ on frequency evolution is illustrated in Fig. 3(e). Obviously, the spectrum width is gradually squeezed from the maximum to single frequency and restored to the maximum expansion. The spectrum width as a function of $\Delta\psi$ is shown in Fig. 3(f). When $\Delta\psi = 0$, the output spectrum width reaches its maximum of 7.06 nm. As the value of $\Delta\psi$ is increased, the spectrum width gradually decreases to zero as $\Delta\psi = \pi$, and then recovers to the widest state at $\Delta\psi = 0$. This result validates that the frequency imaging can be achieved by controlling the pump phase.

C. Frequency shift and negative refraction in the frequency dimension

Next, considering the OFC input, the effects of the synthetic gauge potential on frequency evolution can be further explored. In this case, $\Omega = 54$ GHz and $\Delta\psi$ is fixed. Unlike the case of a single frequency input, the spectrum evolution for an OFC input is determined by the initial Bloch momentum.

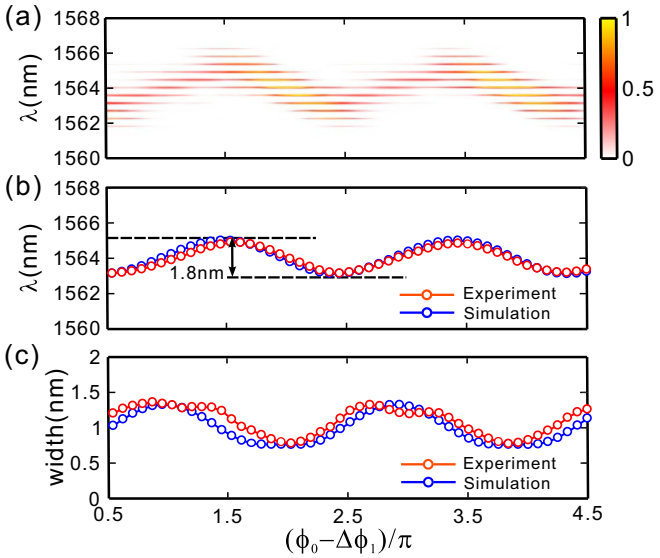

FIG. 5. (a) Experimental result as a function of ϕ_0–$\Delta\phi_1$. (b), (c) Center position and bandwidth of the OFC vs ϕ_0–$\Delta\phi_1$. The orange and blue circles represent the measured and simulated results.

Figures 4(a)–4(c) show the experimental spectrum evolution for $\Delta\psi = 0$. In this case, the band structures of the two processes are identical. Figure 4(a) depicts the measured spectrum for ϕ_0–$\Delta\phi_1 = 0$. With increasing m_d, the spectrum is broadened the same as with the case of a single frequency input. The bandwidth of OFC after the two FWM-BS processes will be larger than 500 GHz. Interestingly, when we change the initial phase ϕ_0–$\Delta\phi_1$ to $-\pi/2$ and $\pi/2$, the frequency evolutions vs m_d manifest the red- and blueshift, shown in Figs. 4(b) and 4(c). The maximum of the accumulated spectral shift approximately reaches 216 GHz ($\Delta\lambda \approx 1.7$ nm), which equals four frequency periods. If the gauge potential in two FWM-BS processes is different, that is, $\Delta\psi = \pi$, the frequency evolution will not continually expand or directionally shift. As ϕ_0–$\Delta\phi_1 = 0$, the OFC first experiences an expansion and then is squeezed to the initial envelope, as shown in Fig. 4(d). Besides, as ϕ_0–$\Delta\phi_1 = -\pi/2$ or $\pi/2$, the frequency envelope experiences a red- or blueshift at first and then recovers to its origin, as depicted in Figs. 4(e) and 4(f), showing a negative refraction effect in the frequency dimension. The experimental and simulated spectra at $m_d = 0$, 1.08, and 2.16 are also depicted in Figs. 4(a)–4(f); obviously, they are in excellent agreement.

Furthermore, we also investigate the spectrum evolution under different gauge potentials for the incidence of OFC when only considering one FWM-BS process in HNLF2 of 400 m. During the experiment, the total power of the pumps has been modulated to 26.05 dBm by EDFA to ensure the conversion efficiency. Through continuously varying ϕ_0–$\Delta\phi_1$ from 0.5π to 4.5π, the trajectory of the spectrum follows periodically the cosine oscillation, as shown in Fig. 5(a). In particular, the spectral red- and blueshift always reach the maximum as ϕ_0–$\Delta\phi_1 = (2j+1)\pi/2$ $(j = 0, 1, 2, \cdots)$ which agrees well with the result of Eq. (6). In addition, the spectral center position ω_c and bandwidth ω_d of the finite-width OFC can be calculated by [47]

$$\omega_c = \frac{\int_{-\infty}^{+\infty} \omega_n |a_n|^2 d\omega}{\int_{-\infty}^{+\infty} |a_n|^2 d\omega}, \tag{7}$$

$$\omega_d = \sqrt{\frac{2\int_{-\infty}^{+\infty} (\omega_n - \omega_c)|a_n|^2 d\omega}{\int_{-\infty}^{+\infty} |a_n|^2 d\omega}}, \tag{8}$$

where ω_n and a_n, respectively, denote the frequency and amplitude of the nth-order idlers. The experimental and simulated calculation results are plotted in Figs. 5(b) and 5(c), which also exhibit periodical oscillations with ϕ_0–$\Delta\phi_1$. As shown in Figs. 5(b) and 5(c), the bandwidth varies between 0.56 and 1.54 nm and the maximum spectral shift can reaches as large as 225 GHz (∼1.8 nm in wavelength). The effect of periodical red and blue spectral shift stems from the band structure of an infinite-width OFC. As the initial Bloch momentum ϕ_0–$\Delta\phi_1$ continuously varies along the whole Brillouin zone, the direction of group velocity will change periodically according to the shape of the band structure, resulting in a periodical oscillation of the spectrum. In addition, if the initial Bloch momentum is fixed, the direction of the group velocity will remain unchanged in the propagation. Thus, the spectrum will experience directional shift as discussed in Fig. 4.

IV. CONCLUSIONS

In summary, we have theoretically established and experimentally demonstrated the effects of diffraction and refraction in frequency dimension by the FWM-BS process in the optical fiber communication system. We have shown that the evolution of the spectrum can be flexibly and efficiently manipulated through the photonic gauge potential introduced by the phase difference of pumps. By varying the gauge potential, we can obtain the directional frequency shift for a frequency comb input and discrete diffraction for a single frequency input. The maximum frequency shift is larger than 200 GHz and the bandwidth expansion can be up to terahertz. Additionally, by cascading two FWM-BS processes with opposite phase differences between two pumps, the negative refraction for the frequency comb and perfect imaging for a single frequency can be achieved in the frequency dimension. Our study may pave the way towards all-optical manipulation of the light spectrum and may find applications in optical communication and signal processing, such as a large bandwidth frequency shifter and frequency multiplexing, temporal-spectral imaging, and spectral domain stealth technology.

ACKNOWLEDGMENTS

The work is supported by the National Natural Science Foundation of China (Grants No. 11974124, No. 11947209, No. 12021004, No. 61735006, and No. 11674117), National Postdoctoral Program for Innovative Talent (BX20190129), and Chinese Postdoctoral Science Foundation General Program (Grant No. 2019M660180).

APPENDIX: COUPLED-MODE EQUATION IN THE FREQUENCY LATTICE

In this Appendix, we provide the detailed derivation of the discrete frequency diffraction in the nonlinear fiber system. We first assume that the wave functions of the signal and pumps are given by

$$a(z,t) = \sum_{n=-\infty}^{\infty} a_n(z) e^{-i\omega_n t}, \tag{A1}$$

$$A(z,t) = A_1(z) e^{-i(\omega_{p1} t + \phi_1)} + A_2(z) e^{-i(\omega_{p2} t + \phi_2)}, \tag{A2}$$

where $a_n(z)$ denotes the amplitudes of the nth-order idler. $A_{1,2}(z)$ are the amplitudes of the two pumps whose incident phases are $\phi_{1,2}$. The frequency of the nth-order idler can be described by $\omega_n = \omega_0 + n\Omega$ $(n = 0, \pm 1, \pm 2, \ldots)$ where ω_0 and Ω denote the frequency of the input signal and the lattice constant. The frequency of the two pumps are ω_{p1} and ω_{p2}, and $\omega_{p1} - \omega_{p2} = \Omega$. During the propagation, the total field in the fiber can be expressed by

$$U = a(z,t) + A(z,t). \tag{A3}$$

The FWM-BS process is governed by the nonlinear Schrödinger equation [46],

$$\frac{\partial U}{\partial z} = i\gamma |U|^2 U, \tag{A4}$$

where γ is the nonlinear coefficient of the HNLF. Using the undepleted pump approximation in which the amplitudes of thepump lights are treated as constants. Substituting Eqs. (S1)–(S3) into Eq. (S4), we can obtain the evolution of signal along z according to the nonlinear Schrödinger equation,

$$\frac{\partial a(z,t)}{\partial z} = 2i\gamma |A(t,0)|^2 a(z,t), \tag{A5}$$

considering that the frequency interval between the two pumps provides the lattice constant of the frequency lattice; thus the right side of Eq. (S5) can be rewritten as

$$\sum_{n=-\infty}^{\infty} [2A_1(0)A_2(0) e^{i(\phi_2 - \phi_1)} a_n(z) e^{-i\omega_{n-1} t} + 2A_1(0)A_2(0) e^{i(\phi_1 - \phi_2)} a_n(z) e^{-i\omega_{n+1} t}]. \tag{A6}$$

By substituting $n \pm 1$ into n, we have

$$\frac{\partial a_n(z)}{\partial z} = 2i\gamma A_1(0)A_2(0)[e^{i(\phi_2 - \phi_1)} a_{n+1}(z) + e^{i(\phi_1 - \phi_2)} a_{n-1}(z)]. \tag{A7}$$

We then define $C = 2\gamma A_1(0)A_2(0)$ and $\Delta\phi = \phi_1 - \phi_2$ as the coupling strength between adjacent modes and the phase difference between the two pumps. Finally, we can obtain the coupled-mode equation for the idlers:

$$\frac{\partial a_n(z)}{\partial z} = 2C[a_{n+1}(z) e^{-i\Delta\phi} + a_{n-1}(z) e^{i\Delta\phi}]. \tag{A8}$$

[1] N. Picqué and T. W. Hänsch, Nat. Photonics **13**, 146 (2019).
[2] A. L. Gaeta, M. Lipson, and T. J. Kippenberg, Nat. Photonics **13**, 158 (2019).
[3] T. Udem, R. Holzwarth, and T. W. Hänsch, Nature **416**, 233 (2002).
[4] S. T. Cundif and J. Ye, Rev. Mod. Phys. **75**, 325 (2003).
[5] T. Fortier and E. Baumann, Commun. Phys. **2**, 153 (2019).
[6] Z. Jiang, D. S. Seo, D. E. Leaird, and A. M. Weiner, Opt. Lett. **30**, 1557 (2005).
[7] D. Z. Kandula, C. Gohle, T. J. Pinkert, W. Ubachs, and K. S. E. Eikema, Phys. Rev. Lett. **105**, 063001 (2010).
[8] K. Predehl, G. Grosche, S. M. F. Raupach, S. Droste, O. Terra, J. Alnis, T. Legero, T. W. Hänsch, T. Udem, R. Holzwarth, and H. Schnatz, Science **336**, 441 (2012).
[9] O. Kliebisch, D. C. Heinecke, S. Barbieri, G. Santarelli, H. Li, C. Sirtori, and T. Dekorsy, Optica **5**, 1431 (2018).
[10] E. Temprana, E. Myslivets, B.P.-P. Kuo, L. Liu, V. Ataie, N. Alic, and S. Radic, Science **348**, 1445 (2015).
[11] V. T. Company, J. Schröder, A. Fülöp, M. Mazur, L. Lundberg, Ó. B. Helgason, M. Karlsson, and P. A. Andrekson, J. Lightwave Technol. **37**, 1663 (2019).
[12] T. J. Kippenberg, R. Holzwarth, and A. Diddams, Science **332**, 555 (2011).
[13] I. Coddington, W. C. Swann, and N. R. Newbury, Phys. Rev. Lett. **100**, 013902 (2008).
[14] J. Morgenweg, I. Barmes, and K. Eikema, Nat. Phys. **10**, 30 (2014).
[15] A. Cingöz, D. C. Yost, T. K. Allison, A. Ruehl, M. E. Fermann, I. Hartl, and J. Ye, Nature **482**, 68 (2012).
[16] P. Maddaloni, M. Bellini, and P. De Natale, *Laser-Based Measurements for Time and Frequency Domain Applications* (CRC Press, Boca Raton, FL, 2013).
[17] C. Qin, L. Yuan, B. Wang, S. Fan, and P. Lu, Phys. Rev. A. **97**, 063838 (2018).
[18] L. Ding, C. Qin, F. Zhou, L. Yang, W. Li, F. Luo, J. Dong, B. Wang, and P. Lu, Phys. Rev. Appl. **12**, 024027 (2019).
[19] A. Regensburger, C. Bersch, M. A. Miri, G. Onishchukov, D. N. Christodoulides, and U. Peschel, Nature **488**, 167 (2012).
[20] H. Chen, C. Qin, B. Wang, and P. Lu, Opt. Lett. **44**, 363 (2019).
[21] S. Wang, C. Qin, B. Wang, and P. Lu, Opt. Express **26**, 19235 (2018).
[22] Q. Lin, X. Q. Sun, M. Xiao, S. C. Zhang, and S. Fan, Sci. Adv. **4**, eaat2774 (2018).
[23] A. Dutt, Q. Lin, L. Yuan, M. Minkov, M. Xiao, and S. Fan, Science **367**, 59 (2020).
[24] L. Yuan, Y. Shi, and S. Fan, Opt. Lett. **41**, 741 (2016).
[25] W. Li, C. Qin, T. Han, H. Chen, B. Wang, and P. Lu, Opt. Lett. **44**, 5430 (2019).
[26] L. Yuan, Q. Lin, M. Xiao, and S. Fan, Optica **5**, 1396 (2018).
[27] X.-W. Luo, X. Zhou, J.-S. Xu, C.-F. Li, G.-C. Gou, C. Zhang, and Z.-W. Zhou, Nat. Commun. **8**, 16097 (2017).

[28] J. Azaña and H. Guillet de Chatellus, Phys. Rev. Lett. **112**, 213902 (2014).
[29] L. Yuan, Q. Lin, A. Zhang, M. Xiao, X. Chen, and S. Fan, Phys. Rev. Lett. **122**, 083903 (2019).
[30] C. Qin, F. Zhou, Y. Peng, D. Sounas, X. Zhu, B. Wang, J. Dong, X. Zhang, A. Alù, and P. Lu, Phys. Rev. Lett. **120**, 133901 (2018).
[31] A. Dutt, M. Minkov, and S. Fan, Light Sci. Appl. **9**, 131 (2020).
[32] Q. Lin, M. Xiao, L. Yuan, and S. Fan, Nat. Commun. **7**, 13731 (2016).
[33] K. Fang, Z. Yu, and S. Fan, Phys. Rev. Lett. **108**, 153901 (2012).
[34] E. Li, B. J. Eggleton, K. Fang, and S. Fan, Nat. Commun. **5**, 3225 (2014).
[35] Q. Lin and S. Fan, Phys. Rev. X **4**, 031031 (2014).
[36] L. Yuan and S. Fan, Optica **3**, 1014 (2016).
[37] C. Bersch, G. Onishchukov, and U. Peschel, Opt. Lett. **34**, 2372 (2009).
[38] B. A. Bell, K. Wang, A. S. Solntsev, D. N. Neshev, A. A. Sukhorukov, and B. J. Eggleton, Optica **4**, 1433 (2107).
[39] K. Wang, B. A. Bell, A. S. Solntsev, D. N. Neshev, B. J. Eggleton, and A. A. Sukhorukov, Light Sci. Appl. **9**, 132 (2020).
[40] J. G. Titchener, B. A. Bell, K. Wang, A. S. Solntsev, B. J. Eggleton, and A. A. Sukhorukov, APL Photonics **5**, 030805 (2020).
[41] K. Li, H. F. Ting, M. A. Foster, and A. C. Foster, Opt. Lett. **41**, 3320 (2016).
[42] A. Cerqueira S. Jr., J. M. Chavez Boggio, A. A. Rieznik, H. E. Hernandez-Figueroa, H. L. Fragnito, and J. C. Knight, Opt. Express **16**, 2816 (2008).
[43] I. Agha, M. Davanco, B. Thurston, and K. Srinivasan, Opt. Lett. **37**, 2997 (2012).
[44] K. Li, H. Sun, and A. C. Foster, Opt. Lett. **42**, 1488 (2017).
[45] Q. Li, M. Davanço, and K. Srinivasan, Nat. Photonics **10**, 406 (2016).
[46] G. P. Agrawal, *Nonlinear Fiber Optics* (Academic Press, New York, 2007).
[47] T. Han, H. Chen, C. Qin, W. Li, B. Wang, and P. Lu, Phys. Rev. A **97**, 063815 (2018).